Editors' Suggestion

Deexcitation Dynamics of Muonic Atoms Revealed by High-Precision Spectroscopy of Electronic K X Rays

T. Okumura,[1,*] T. Azuma,[1,†] D. A. Bennett,[2] P. Caradonna,[3] I. Chiu,[4] W. B. Doriese,[2] M. S. Durkin,[2] J. W. Fowler,[2] J. D. Gard,[2] T. Hashimoto,[5] R. Hayakawa,[6] G. C. Hilton,[2] Y. Ichinohe,[7] P. Indelicato,[8] T. Isobe,[9] S. Kanda,[10] D. Kato,[11] M. Katsuragawa,[3] N. Kawamura,[10] Y. Kino,[12] M. K. Kubo,[13] K. Mine,[3] Y. Miyake,[10] K. M. Morgan,[2] K. Ninomiya,[4] H. Noda,[14] G. C. O'Neil,[2] S. Okada,[1,‡] K. Okutsu,[12] T. Osawa,[15] N. Paul,[8] C. D. Reintsema,[2] D. R. Schmidt,[2] K. Shimomura,[10] P. Strasser,[10] H. Suda,[6] D. S. Swetz,[2] T. Takahashi,[3] S. Takeda,[3] S. Takeshita,[10] M. Tampo,[10] H. Tatsuno,[6] X. M. Tong,[16] Y. Ueno,[1] J. N. Ullom,[2] S. Watanabe,[17] and S. Yamada[7]

[1]*Atomic, Molecular and Optical Physics Laboratory, RIKEN, Wako 351-0198, Japan*
[2]*National Institute of Standards and Technology, Boulder, Colorado 80305, USA*
[3]*Kavli IPMU (WPI), The University of Tokyo, Kashiwa, Chiba 277-8583, Japan*
[4]*Department of Chemistry, Osaka University, Toyonaka, Osaka 560-0043, Japan*
[5]*Advanced Science Research Center (ASRC), Japan Atomic Energy Agency (JAEA), Tokai 319-1184, Japan*
[6]*Department of Physics, Tokyo Metropolitan University, Tokyo 192-0397, Japan*
[7]*Department of Physics, Rikkyo University, Tokyo 171-8501, Japan*
[8]*Laboratoire Kastler Brossel, Sorbonne Université, CNRS, ENS-PSL Research University, Collège de France, Case 74, 4, place Jussieu, 75005 Paris, France*
[9]*RIKEN Nishina Center, RIKEN, Wako 351-0198, Japan*
[10]*High Energy Accelerator Research Organization (KEK), Tsukuba, Ibaraki 305-0801, Japan*
[11]*National Institute for Fusion Science (NIFS), Toki, Gifu 509-5292, Japan*
[12]*Department of Chemistry, Tohoku University, Sendai, Miyagi 980-8578, Japan*
[13]*Department of Natural Sciences, College of Liberal Arts, International Christian University, Mitaka, Tokyo 181-8585, Japan*
[14]*Department of Earth and Space Science, Osaka University, Toyonaka, Osaka 560-0043, Japan*
[15]*Materials Sciences Research Center (MSRC), Japan Atomic Energy Agency (JAEA), Tokai 319-1184, Japan*
[16]*Center for Computational Sciences, University of Tsukuba, Tsukuba, Ibaraki 305-8573, Japan*
[17]*Department of Space Astronomy and Astrophysics, Institute of Space and Astronautical Science (ISAS), Japan Aerospace Exploration Agency (JAXA), Sagamihara, Kanagawa 252-5210, Japan*

(Received 12 February 2021; accepted 11 June 2021; published 27 July 2021)

We observed electronic K x rays emitted from muonic iron atoms using superconducting transition-edge sensor microcalorimeters. The energy resolution of 5.2 eV in FWHM allowed us to observe the asymmetric broad profile of the electronic characteristic $K\alpha$ and $K\beta$ x rays together with the hypersatellite $K^h\alpha$ x rays around 6 keV. This signature reflects the time-dependent screening of the nuclear charge by the negative muon and the L-shell electrons, accompanied by electron side feeding. Assisted by a simulation, these data clearly reveal the electronic K- and L-shell hole production and their temporal evolution on the 10–20 fs scale during the muon cascade process.

DOI: 10.1103/PhysRevLett.127.053001

A muonic atom is a bound state consisting of a negative muon and a nucleus, sometimes accompanied by bound electrons. Because of the larger muon mass, the Bohr radius is about 207 times smaller than that of the electron. Because of the screening effect when the muon is in its $1s$ ground state, the electron shell is well approximated by that of a $Z-1$ nucleus. After its formation, the muonic atom survives for a finite time before the muon is captured by the nucleus, normally on a timescale shorter than the 2.2 μs intrinsic lifetime of the negative muon. Research on muonic atoms has been pursued by the atomic, nuclear, and particle physics communities for many decades [1–3], and muonic atom x-ray spectroscopy has been widely applied to determine nuclear sizes and shapes [4–7]. Measurements of the proton size using muonic hydrogen and deuterium have spurred the so-called "proton radius puzzle" and a host of beyond standard model physics proposals [8–12]. Recently muonic atoms have been proposed as a new testing ground for bound-state quantum electrodynamics [13]. In addition to these fundamental questions of quantum structure, the dynamical aspect of the electronic cloud in muonic atoms poses a fascinating quantum few-body problem, of which little is known, though some parallels may be drawn with the deexcitation dynamics of highly charged ions in solids or during ion-surface interactions [14–18].

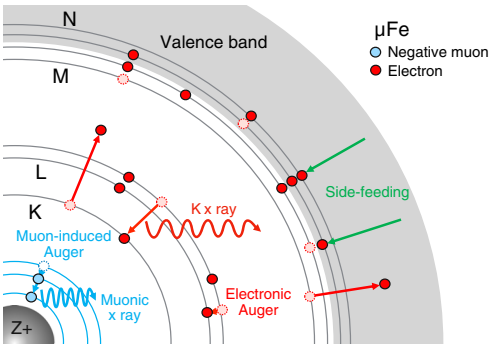

FIG. 1. Schematic drawing of the muon cascade process with the electron configuration evolution in the muonic iron atom (μFe) in Fe metal. Side feeding and electron refilling *via* radiative decay or electronic Auger decay fill the electron holes. All scales are arbitrary. We assume that the number of $4s$ electrons is a constant during the cascade because of rapid N-shell side feeding.

When a negative muon is captured by an atom, normally in a highly excited state, the muon starts to cascade towards the nucleus first by muon-induced Auger decay (stripping bound electrons), and then *via* radiative decay (emitting muonic x rays). The former process dominates at the beginning of the cascade, accompanying electron ejection from M shell, followed by L shell and K shell. The latter radiative decay is important when the muon approaches the lower levels. Finally, the muon reaches the atomic $1s$ ground state. When an electronic hole is formed during the muon cascade process, electronic characteristic x rays are also emitted as shown schematically in Fig. 1. The time-scale of the cascade process is typically $\sim$10 fs for elemental Fe, while the $1s$ muon capture rate by the Fe nucleus is 4.4×10^6 s^{-1} [19]. Thus, the majority of muons are captured from the atomic $1s$ ground state. When the muonic atom is formed inside a solid-state target, electron side feeding from the surrounding environment also takes place [20].

Historically, the muon cascade process has been studied by examining the intensity distribution of the muonic x-ray line series, and is often compared with the cascade simulation originally developed by Vogel *et al.* [21–26] and by Hartmann *et al.* [20,27,28]. It was found that muons capture onto orbitals with principal quantum numbers above $n = 20$, and that the ℓ distribution is somewhat modified from the statistical one. The muonic x-ray spectroscopy also encodes information on the bound electrons, as the screening of the nuclear charge by these electrons modifies the muonic x-ray energies [29–31].

The electron hole filling by the upper-level electrons *via* radiative decay or electronic Auger decay (hereafter called electron refilling), and side feeding from the surrounding medium are also of critical interest. In a solid-state target, electron side feeding is unavoidable [2], and in gas targets there is a pressure dependence of the collisional charge transfer that was carefully studied in the 1980s and 1990s [32–34]. Since then, however, little substantial progress has been made, and a detailed understanding of electron dynamics in the muonic atom including the muon-induced Auger effect, refilling, and side feeding remains elusive.

The observation of the *electronic* characteristic x rays from the muonic atom is an alternative, powerful approach to shed light on the cascade dynamics. When an electron hole is formed in the K shell by the muon-induced Auger process, the corresponding electronic K x ray is emitted. It is naturally expected that electronic K x rays may be a particularly sensitive probe for the electron dynamics because the electron-electron interaction contributes more significantly to the energy of the K x rays than the muonic x rays. The dependence of the electronic K x-ray energies on the muon state was recognized by pioneering works for heavy elements ($Z > 75$) [35–37], however, the insufficient resolution of the Ge detectors prevented further detailed study.

In this Letter, we report high-precision measurements of electronic K x rays emitted from muonic iron atoms (μFe) using state-of-the-art superconducting transition-edge sensor (TES) microcalorimeters, which utilize the steep temperature dependence of resistance at the superconducting phase transition [38]. The μFe atoms were produced in a metallic Fe target in the region close to the surface by a slow negative muon beam of 20.5 MeV/c (peak stopping depth = 20 μm). This condition enables the emission of corresponding electronic K x rays into vacuum with minimal self-absorption (half-absorption length = 10 μm). The electronic $K\alpha$ and $K\beta$ x rays were observed at an energy around 6 keV, which is close to the characteristic x rays of the $Z-1$ atom, i.e., manganese (Mn), due to the screening of the nuclear charge by the muon. The high resolution (5.2 eV in FWHM) TES detector revealed that the K x-ray spectrum is asymmetric and widely broadened with a width of about 200 eV. Furthermore, we clearly observed a peak corresponding to hypersatellite $K^h\alpha$ x rays from the double K-hole state. The energy of the electronic x rays strongly depends both on the muon state and the electron configuration at the time of electronic x-ray emission, thus the overall shape of the spectrum reflects the electron dynamics including electron hole production, refilling and side-feeding during the muon cascade process. We calculated these energy shifts and developed a theoretical evolution model. By comparing the measured spectrum with the simulation we can provide a clear picture of the relevant exotic atom dynamics.

The measurement was carried out at the D2 beam line of the Materials and Life Science Experimental Facility (MLF) at J-PARC [39]. Details of the experimental setup may be found in the previous technical papers [40,41]. Briefly, the low-momentum negative muons (20.5 MeV/c) were stopped in a 100 μm-thick Fe foil after passing through thin Kapton foils and an air gap. The TES x-ray detector was placed normal to the muon-beam

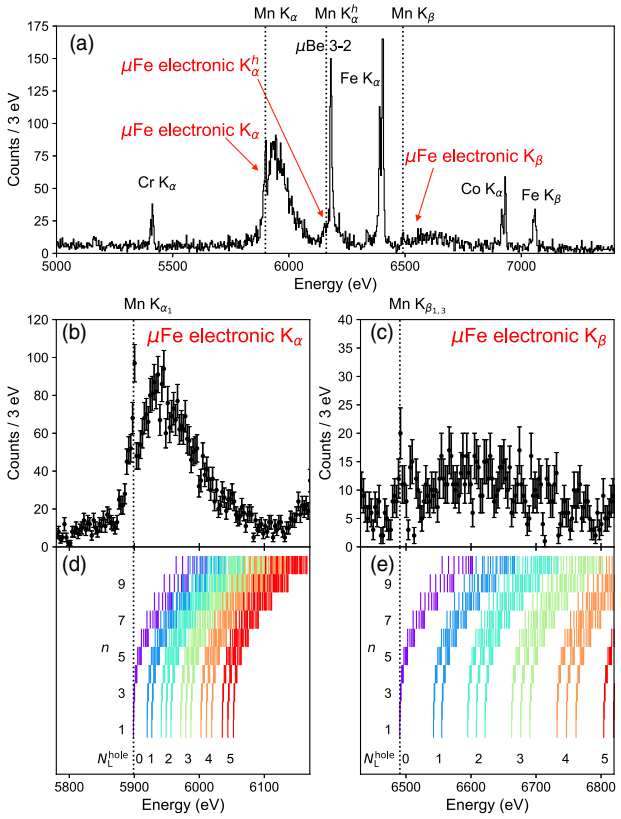

FIG. 2. (a) X-ray spectrum in the energy range from 5000 to 7400 eV measured by the TES detector. Broad electronic $K\alpha$ and $K\beta$ x rays from μFe are observed. In addition, sharp Mn $K\alpha 1$ and $K\beta 1,3$ x rays are identified (dotted lines). The Mn $K\alpha 2$ x rays are discernible at the low-energy side of the Mn $K\alpha 1$ line. Muonic x rays from μBe ($n = 3 \rightarrow 2$) are due to direct muon injection into a Be window in front of the detector. A broad tail-like structure beneath the peak of muonic x rays from μBe is identified as the hypersatellite $K^h\alpha$ x rays. The energy of Mn $K^h\alpha$ is also shown [58]. Cr and Co $K\alpha$ x rays are calibration x rays from the x-ray generator. Fe $K\alpha$ and $K\beta$ x rays are due to direct injection of muons and background particles into the Fe target. Expanded spectra for (b) electronic $K\alpha$ x rays and (c) electronic $K\beta$ x rays from μFe. (d) Calculated $K\alpha$ and (e) $K\beta$ x-ray energies under different muon states (n) and electron configurations with L holes ($N_L^{\rm hole}$). See details in the main text. Regarding the muonic ℓ level, only the case of $\ell = n - 1$ is shown for clarity.

direction and 75 mm away from the target position. The Fe foil was tilted by 45° with respect to the muon-beam direction. The muons were delivered in a double-pulse structure, with $\sim 1 \times 10^4$ muons per double pulse. Each pulse had a width of 100 ns, and the double pulses had a repetition rate of 25 Hz. The x-ray energy and detection time with respect to the pulsed muon beam injection were simultaneously accumulated [40]. We estimated that the negative muons were stopped at around 20 μm from the surface of the foil, so that a large fraction of the ~6 keV x rays traversed the foil [42].

The x-ray detector is based on a 240-pixel TES array developed by the National Institute of Standards and Technology (NIST) [52]. The TES system, cooled with a pulse-tube-backed adiabatic demagnetization refrigerator (ADR), is identical to the system we employed for the pionic atom experiment at the Paul Scherrer Institute and the kaonic atom experiment at J-PARC [53–55]. Each pixel contains a TES consisting of a bilayer of thin Mo/Cu films whose superconducting critical temperature is about 107 mK, and a 4 μm-thick Bi absorber for converting an x-ray energy into heat. The TES can detect x rays up to 10 keV, and the absorption efficiency of the Bi layer is 85% at 6 keV. The effective area of each pixel is 305×290 μm^2 and the total active area of the array is about 23 mm^2. Energy calibration of the TES detector was performed by using an x-ray generator installed at the front of the detector. The characteristic x rays from Cr, Co, and Cu were used as calibration x-ray lines. The number of employed pixels of the TES array was restricted to 197 by the geometrical configuration. The energy accuracy as determined by the absolute position of the Fe $K\alpha$ line is better than 0.6 eV.

Figure 2(a) shows the full spectrum, obtained by summing data from all pixels and applying a time cut to extract the beam-induced signals. The energy resolution was evaluated to be 5.2 eV (FWHM) in this energy regime using Co $K\alpha 1$ and $K\alpha 2$ x rays. The energy, width, and shape used to derive the resolution and energy calibration are evaluated using the accurate parameters provided in Ref. [56] for the Cr, Co, and Cu $K\alpha/K\beta$ lines, corrected for new fundamental constants and crystal parameters following Ref. [57]. A remarkable asymmetric broad peak of electronic $K\alpha$ x rays from μFe is observed, starting from the energies of electronic Mn $K\alpha 1$ and $K\alpha 2$ x-ray lines at 5899 and 5888 eV, respectively, and extending across 200 eV [Fig. 2(b)]. A similar structure for electronic $K\beta$ x rays from μFe is identified, which starts from the energy of an electronic Mn $K\beta$ x-ray line at 6490 eV [Fig. 2(c)]. We also observed a broad tail-like structure beneath the peak of muonic x rays from μBe at 6179 eV [Fig. 2(a)], which was determined to be the hypersatellite $K^h\alpha$ x rays from μFe. This structure starts from the energies of Mn $K^h\alpha 2$ at 6143.4 eV [58].

These peaks disappeared from the spectrum for the 26.0 MeV/c muon beam. This observation is convincing evidence that the electronic K x rays come from μFe. They were completely attenuated because of the self-absorption due to the increased muon penetration depth.

The Mn $K\alpha$ and $K\beta$ x-ray lines originate after the muon is captured by the Fe nucleus. The resulting Mn nucleus deexcites through the internal conversion process, leading to delayed K-shell hole production followed by Mn K x-ray emission, as shown by Schneuwly and Vogel for high-Z muonic atoms [37]. Because the nuclear capture rate is slow, all electronic holes of μFe are filled *via* refilling and side feeding before the capture. Thus, the Mn K x rays do not show broadening like the μFe electronic x rays.

As already explained, the energies of the electronic K x rays emitted from μFe during the cascade process are affected both by the muon screening and by the electron configuration at the moment of x-ray emission, which depend on the evolution of the deexcitation dynamics. To evaluate these contributions, we calculated the energy structure of the electronic K x rays employing the strategy already developed for highly charged hollow ions in the bulk of metallic materials [59]. We calculated the total energies of μFe in vacuum with nonrelativistic density functional theory and an optimized effective potential considering the self-interaction corrections [60]. We considered the muon to be moving in an effective potential generated by the nucleus and the surrounding electrons, and the electrons moving in an effective potential of the nucleus and the muon, self-consistently. The number of possible configurations with different muon states and electron occupancies in the K, L, and M shells is close to 30 000. The K x-ray energies are obtained by the total energy difference of the two configurations involved in the transitions. We found that the outer screening effect by the surrounding metal is less important for the present μFe case, because the valence band formed by the $3d$ and $4s$ electrons is located close to the vacuum level, while K- and L-shell electrons are deeply bound by the muon-screened nucleus, leading to a negligibly small interaction.

Note that in order to compare with the measured spectra, we shifted the calculated energies by a constant value so that they match the reported ones [56]. This shift is mainly due to relativistic effects. To confirm the validity of our approach we also compared some of the shifted values with the energies from stringent calculations including first and second order QED corrections, the full Breit interaction, all-order retardation, and the finite nuclear size using the MCDFGME code [61,62], which can account for all these effects for exotic atoms with an arbitrary number of remaining electrons [63–65]. Correlation, Auger shift and core-core correlation contributions for inner shell holes [66] are not included, but as can be seen in Ref. [66] they partially cancel out and should not contribute more than 2–3 eV to the shift. The difference is not constant but depends on the transitions; nevertheless, it is less than 10 eV, which is small compared to the 200 eV width of the μFe K x-ray spectra. Thus, for the present discussion, we treated the difference as a constant shift [42].

The calculated μFe $K\alpha$ and $K\beta$ x-ray energies are shown in Figs. 2(d) and 2(e), respectively, for a variety of muon quantum numbers and electron configurations. The K x-ray energy shifts due to larger muon screening at the lower muon levels (n) are clearly visible, where perfect screening corresponds to the case of $Z-1$. However the observed width of about 200 eV is not explained exclusively by this shift. The shift due to different electron configurations, which depends particularly on the number of electron holes in the L shell (N_L^{hole}), is also significant. We found a systematic shift to higher energy for large N_L^{hole}. It is also apparent that the n dependence of the energy shift is similar for different N_L^{hole}. We notice that the energy shift of $K\beta$ x rays for the L holes is larger than that of $K\alpha$ x rays [37]. Nevertheless, it is clear that we cannot directly distinguish these two effects simply from the corresponding energies. The observed broadening can be explained by the convolution of these two effects.

The next step is to include the temporal evolution of the muon state and electron configuration. The lifetime of the K hole before filling is 0.59 fs [67], which is much shorter than the typical lifetime (several fs) of the muon occupying the specific state. Thus, the critical issue is the electron configuration of the L shell at the moment when the K hole is produced. An L hole is produced *via* the muon-induced Auger process and refilling of the K hole from the L-shell electron. The resulting L hole is refilled by a Coster-Kronig transition [68], or an M-shell electron. In addition, the electron side feeding from the surrounding also has to be taken into account.

The observed $K\alpha$ spectrum was fitted with the one calculated by the cascade simulation [42], where the M-shell per-hole side-feeding rate Γ_M was treated as a fitting parameter. For normalization, intensities of both the $K\alpha$ x rays from μFe and the Mn $K\alpha$ x rays after the nuclear capture, and a constant background were also treated as fitting parameters. We considered dynamics of electrons in K, L, and M shells. The muon-induced process was dealt with using the Akylas and Vogel's code [25]. We employed the electronic radiative and Auger transition rates from Refs. [69–71], respectively. For the electron side feeding from the surrounding, the electron hole is filled by the valence band electron either *via* Auger or radiative process. The side-feeding rate is dominantly determined by the overlap of the initial and final state wave functions. The wave function of the valence band consists of $3d$ and $4s$ electrons of Fe, forming a hybrid orbital. Therefore, the transition from the valence band to the N shell ($4s$) and M shell plays an important role. In our model we considered only the M-shell side feeding, which is followed by the L-shell refilling from the M shell. Regarding $4s$ holes, the side feeding must be very efficient and we assumed that they are instantly fed from the valence band, i.e., the number of $4s$ electrons is always two during the cascade process. We point out that the Auger process is generally preferred to radiative transitions for mid-Z nuclei, however, we do not need to distinguish between the Auger and the radiative process when the side-feeding rate is a fitting parameter.

Figure 3(a) shows the results for $K\alpha$ x rays. It is clearly seen that the M-shell side-feeding rate changes the whole spectrum drastically, and a simulation neglecting side feeding ($\Gamma_M = 0.0$ fs^{-1}) does not explain the observed feature at all. Thus, we can use the spectrum to study the evolution of the electron configuration by including this side feeding precisely. The best simulated spectrum for $K\alpha$

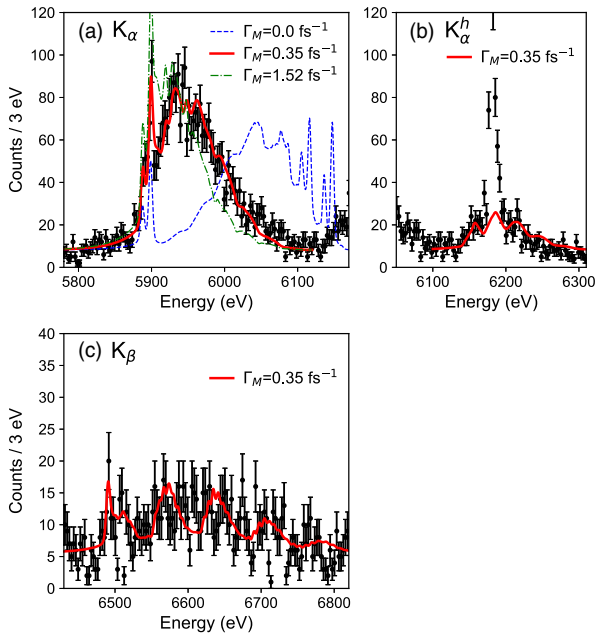

FIG. 3. Comparison of the simulated and corresponding measured K x-ray spectra. The simulated spectra are after convolution by the energy response function of the TES detector. (a) Simulated $K\alpha$ x-ray spectrum with three side-feeding rates ($\Gamma_M = 0.0$, 0.35, and 1.52 fs^{-1}). (b) Simulated hypersatellite $K^h\alpha$ x-ray spectrum under the same parameters as (a) with $\Gamma_M = 0.35$ fs^{-1}. (c) Simulated $K\beta$ x-ray spectrum under the same parameters as (a) with $\Gamma_M = 0.35$ fs^{-1}.

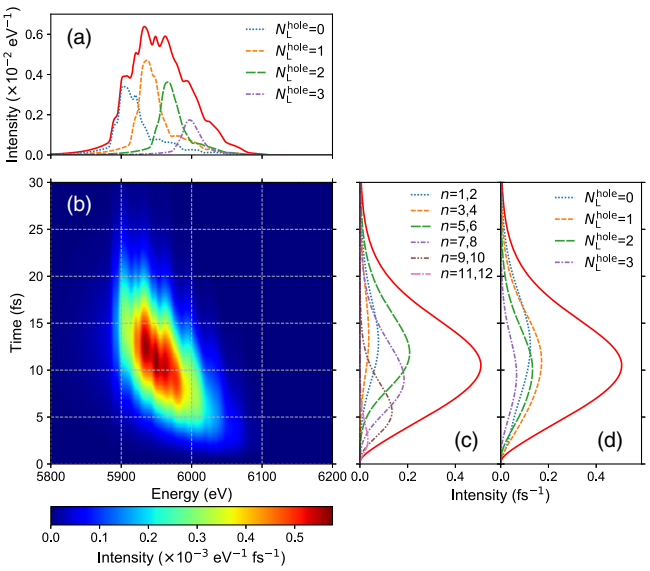

FIG. 4. (a) The simulated N_L^{hole}-resolved $K\alpha$ x-ray spectrum for $\Gamma_M = 0.35$ fs^{-1}. The red curve is the same as the one in Fig. 3(a) except for the Mn $K\alpha$ line. (b) A contour map of the simulated x-ray intensities as functions of the energy and the time after muon capture for $\Gamma_M = 0.35$ fs^{-1}. A detailed definition of the two-dimensional intensities is described in the Supplemental Material [42]. The spectrum (a) is obtained by projection of the contour map into energy direction. (c),(d) The temporal distribution of the n- and N_L^{hole}-resolved x-ray intensities made by projection of (b) on the time axis, respectively.

x rays is reproduced for the side-feeding rate of $\Gamma_M = 0.35(2)$ fs^{-1}. Using exactly the same values of Γ_M and the intensity of the μFe $K\alpha$ x rays, we also reproduced the hypersatellite $K^h\alpha$ x-ray and $K\beta$ x-ray spectra shown in Figs. 3(b) and 3(c), respectively. Here we note that these intensities were corrected using the $K\alpha$ one taking into account self-absorption efficiencies in the Fe target at different energies. The agreement is excellent for all three spectra. We remark that, for the calculation of the hypersatellite $K^h\alpha$ x-ray spectrum, we employed the experimental intensity ratio of $K^h\alpha 1/K^h\alpha 2 = 0.13(1)$ by Diamant *et al.* [58]. It is different from the value of two for the single K-hole state, reflecting the intermediate coupling [58] (see the detail in the Supplemental Material [42]). These features compare well with deexcitation x-ray spectra of highly charged ions accompanied by many K holes and L holes (hollow atoms) [17,18]. The side-feeding effect of highly charged ions in a metal has been extensively studied [72,73]. The side-feeding rate obtained in the present study cannot be directly compared with the results of highly charged ions, because the data for the combination of Mn ions and a Fe target is not available. We found however that they are of the same order of magnitude.

The excellent agreement of the present simulation with the spectrum obtained experimentally strongly supports our interpretation of the involved dynamics. Figure 4(a) shows N_L^{hole}-resolved simulation spectrum indicating that the $K\alpha$ x rays are emitted mainly under the electron configuration of $N_L^{hole} = 0$, 1, 2, and 3. Note that each energy distribution for specific N_L^{hole} has a small tail component on the higher-energy side, which corresponds to K x rays from the high-n state, reflecting the configuration at an early time. More in detail, as shown in Fig. 4(b), we can grasp the dynamics by a contour map of the emitted $K\alpha$ x-ray intensities as functions not only of the x-ray energy but also of the time after muon capture. A negative slope in time vs energy is apparent; the energy shifts lower as time proceeds, reflecting the larger muon screening. Namely, the evolution of the muon state n is regarded as a kind of "clock" in the fs time range. As shown in Fig. 4(c), the majority of the x rays are emitted when the muon is in states from $n = 10$ down to $n = 5$, where K-hole production is expected, and the main events take place between 5 to 20 fs. The temporal evolution of N_L^{hole} is shown in Fig. 4(d); N_L^{hole} increases to ~2 in average, and then gradually decreases. Combining these facts, we conclude that the observed energy distribution clearly reflects the electron configuration.

In summary, we observed the asymmetric broad spectrum of the electronic characteristic $K\alpha$ and $K\beta$ x rays from the single K-hole state of μFe together with the hypersatellite $K^h\alpha$ x rays from the double K-hole state, using a TES detector with ~50 times better resolution than the

conventional semiconductor detector. We made decisive progress towards understanding the temporal evolution of electron dynamics during the muon cascade process, which remained unresolved for decades. This high-precision measurement suggests a new way to revisit dynamics of muonic atoms not only in metals but semiconductors, insulators, and molecules in the near future.

The muon experiment at the Materials and Life Science Experimental Facility of the J-PARC was performed under a user program (2019 MS01). This work was supported by the JSPS KAKENHI (Grant-in-Aid for Scientific Research on Innovative Areas, Toward new frontiers: encounter and synergy of state-of-the-art astronomical detectors and exotic quantum beams 18H05457, 18H05458, 18H05460, 18H05461, 18H05463, and 18H05464, Grant-in-Aid for Scientific Research (A) 18H03713 and 18H03714, and Grant-in-Aid for Young Scientists, 20K14524 and 20K15238), and the RIKEN Pioneering Projects. N. P. thanks CNRS Institute of Physics for support and RIKEN for a young scientist fellowship. X. M. T. was supported by Multidisciplinary Cooperative Research Program in CCS, University of Tsukuba. Y. K. is grateful for the support of the NIFS Collaboration Research Program (NIFS19KKGF043). P. I. is a member of the Allianz Program of the Helmholtz Association, Contract No. EMMI HA-216 "Extremes of Density and Temperature: Cosmic Matter in the Laboratory."

*takuma.okumura@riken.jp
†toshiyuki-azuma@riken.jp
‡Present address: Chubu University, Kasugai, Aichi 487-8501, Japan.

[1] D. Horváth, in *Handbook of Nuclear Chemistry*, 2nd ed., edited by A. Vértes, S. Nagy, Z. Klencsár, R. G. Lovas, and F. Rösch (Springer, Boston, 2011), pp. 1485–1513.
[2] D. Measday, Phys. Rep. **354**, 243 (2001).
[3] T. Gorringe and D. Hertzog, Prog. Part. Nucl. Phys. **84**, 73 (2015).
[4] L. A. Schaller, in *Muonic Atoms and Molecules*, edited by L. A. Schaller and C. Petitjean (Birkhäuser Verlag Basel, Basel, 1993), pp. 89–94.
[5] E. Borie and G. A. Rinker, Rev. Mod. Phys. **54**, 67 (1982).
[6] G. Fricke and K. Heilig, *Nuclear Charge Radii*, Vol. 20 of Landolt-Börnstein—Group 1 Elementary Particles, Nuclei and Atoms (Springer-Verlag, Berlin, 2004).
[7] I. Angeli and K. P. Marinova, At. Data Nucl. Data Tables **99**, 69 (2013).
[8] R. Pohl, A. Antognini, F. Nez, F. D. Amaro, F. Biraben, J. M. R. Cardoso, D. S. Covita, A. Dax, S. Dhawan, L. M. P. Fernandes *et al.*, Nature (London) **466**, 213 (2010).
[9] A. Antognini, F. Nez, K. Schuhmann, F. D. Amaro, F. Biraben, J. M. R. Cardoso, D. S. Covita, A. Dax, S. Dhawan, M. Diepold *et al.*, Science **339**, 417 (2013).
[10] R. Pohl, F. Nez, L. M. P. Fernandes, F. D. Amaro, F. Biraben, J. M. R. Cardoso, D. S. Covita, A. Dax, S. Dhawan, M. Diepold *et al.*, Science **353**, 669 (2016).
[11] J.-P. Karr, D. Marchand, and E. Voutier, Nat. Rev. Phys. **2**, 601 (2020).
[12] J. J. Krauth, K. Schuhmann, M. A. Ahmed, F. D. Amaro, P. Amaro, F. Biraben, T.-L. Chen, D. S. Covita, A. J. Dax, M. Diepold *et al.*, Nature (London) **589**, 527 (2021).
[13] N. Paul, G. Bian, T. Azuma, S. Okada, and P. Indelicato, Phys. Rev. Lett. **126**, 173001 (2021).
[14] M. W. Carlen, M. Polasik, B. Boschung, J.-C. Dousse, M. Gasser, Z. Halabuka, J. Hoszowska, J. Kern, B. Perny, C. Rhême *et al.*, Phys. Rev. A **46**, 3893 (1992).
[15] N. Stolterfoht, in *The Physics of Multiply and Highly Charged Ions*, edited by F. J. Currell (Kluwer Academic Publishers, Netherlands, 2003), Vol. 2, pp. 69–120.
[16] A. Arnau, F. Aumayr, P. Echenique, M. Grether, W. Heiland, J. Limburg, R. Morgenstern, P. Roncin, S. Schippers, R. Schuch *et al.*, Surf. Sci. Rep. **27**, 113 (1997).
[17] J. P. Briand, L. de Billy, P. Charles, S. Essabaa, P. Briand, R. Geller, J. P. Desclaux, S. Bliman, and C. Ristori, Phys. Rev. Lett. **65**, 159 (1990).
[18] J. P. Briand, L. de Billy, P. Charles, S. Essabaa, P. Briand, R. Geller, J. P. Desclaux, S. Bliman, and C. Ristori, Phys. Rev. A **43**, 565 (1991).
[19] T. Suzuki, D. F. Measday, and J. P. Roalsvig, Phys. Rev. C **35**, 2212 (1987).
[20] F. J. Hartmann, in *Muonic Atoms and Molecules*, edited by L. A. Schaller and C. Petitjean (Birkhäuser Verlag Basel, Basel, 1993), pp. 157–165.
[21] P. Vogel, Phys. Rev. A **7**, 63 (1973).
[22] P. Vogel, At. Data Nucl. Data Tables **14**, 599 (1974).
[23] P. Vogel, Phys. Lett. B **58**, 52 (1975).
[24] P. Vogel, A. Zehnder, A. L. Carter, M. S. Dixit, E. P. Hincks, D. Kessler, J. S. Wadden, C. K. Hargrove, R. J. McKee, H. Mes *et al.*, Phys. Rev. A **15**, 76 (1977).
[25] V. R. Akylas and P. Vogel, Comput. Phys. Commun. **15**, 291 (1978).
[26] P. Vogel, Phys. Rev. A **22**, 1600 (1980).
[27] F. J. Hartmann, T. von Egidy, R. Bergmann, M. Kleber, H. J. Pfeiffer, K. Springer, and H. Daniel, Phys. Rev. Lett. **37**, 331 (1976).
[28] F. J. Hartmann, R. Bergmann, H. Daniel, H. J. Pfeiffer, T. Egidy, and W. Wilhelm, Z. Phys. A **305**, 189 (1982).
[29] L. Simons, D. Abbot, B. Bach, R. Bacher, A. Badertscher, P. Blüm, P. DeCecco, J. Eades, J. Egger, K. Elsener *et al.*, Nucl. Instrum. Methods Phys. Res., Sect. B **87**, 293 (1994).
[30] I. Beltrami, B. Aas, W. Beer, P. Ebersold, R. Eichler, P. F. A. Goudsmit, M. Guanziroli, T. v. Ledebur, H. J. Leisi, W. Ruckstuhl *et al.*, Nucl. Phys. **A429**, 381 (1984).
[31] I. Beltrami, B. Aas, W. Beer, G. De Chambrier, P. F. A. Goudsmit, T. v. Ledebur, H. J. Leisi, W. Ruckstuhl, W. W. Sapp, G. Strassner *et al.*, Nucl. Phys. **A451**, 679 (1986).
[32] R. Bacher, D. Gotta, L. M. Simons, J. Missimer, and N. C. Mukhopadhyay, Phys. Rev. Lett. **54**, 2087 (1985).
[33] R. Bacher, P. Blüm, D. Gotta, K. Heitlinger, M. Schneider, J. Missimer, and L. M. Simons, Phys. Rev. A **39**, 1610 (1989).

[34] K. Kirch, D. Abbott, B. Bach, P. Hauser, P. Indelicato, F. Kottmann, J. Missimer, P. Patte, R. T. Siegel, L. M. Simons *et al.*, Phys. Rev. A **59**, 3375 (1999).

[35] R. Arlt, Z. Ganzorik, T. Krogulski, H.-G. Ortlepp, S. M. Polikanov, B. M. Sabirov, V. D. Fromm, U. Schmidt, G. Schnefli, and R. Engfer, JETP Lett. **20**, 291 (1974).

[36] W. D. Fromm, D. Gansorig, T. Krogulski, H.-G. Ortlepp, S. M. Polikanov, B. M. Sabirov, U. Schmidt, R. Arlt, R. Engfer, and H. Scheuwly, Phys. Lett. B **55**, 377 (1975).

[37] H. Schneuwly and P. Vogel, Phys. Rev. A **22**, 2081 (1980).

[38] J. N. Ullom and D. A. Bennett, Supercond. Sci. Technol. **28**, 084003 (2015).

[39] W. Higemoto, R. Kadono, N. Kawamura, A. Koda, K. Kojima, S. Makimura, S. Matoba, Y. Miyake, K. Shimomura, and P. Strasser, Quantum Beam Sci. **1**, 11 (2017).

[40] S. Okada, T. Azuma, D. A. Bennett, P. Caradonna, W. B. Doriese, M. S. Durkin, J. W. Fowler, J. D. Gard, T. Hashimoto, R. Hayakawa *et al.*, J. Low Temp. Phys. **200**, 445 (2020).

[41] T. Okumura, T. Azuma, D. A. Bennett, P. Caradonna, I.-H. Chiu, W. B. Doriese, M. S. Durkin, J. W. Fowler, J. D. Gard, T. Hashimoto *et al.*, IEEE Trans. Appl. Supercond. **31**, 1 (2021).

[42] See Supplemental Material at http://link.aps.org/supplemental/10.1103/PhysRevLett.127.053001 for the simulation of the muon stopping position, which includes Refs. [43,44], for the theoretical calculation the K x-ray energies, which includes Refs. [45–47], and the cascade simulation, which includes Refs [48–51].

[43] Geant4, https://geant4.web.cern.ch.

[44] J. H. Hubbel and S. M. Seltzer, Tables of X-Ray Mass Attenuation Coefficients and Mass Energy-Absorption Coefficients, NIST Standard Reference Database 126 (2004), http://physics.nist.gov/xaamdi.

[45] X.-M. Tong and S.-I. Chu, Phys. Rev. A **57**, 855 (1998).

[46] P. Indelicato and E. Lindroth, Phys. Rev. A **46**, 2426 (1992).

[47] T. Mukoyama, Eur. Phys. J. D **73**, 75 (2019).

[48] M. H. Chen, Phys. Rev. A **44**, 239 (1991).

[49] V. L. Jacobs, J. Davis, B. F. Rozsnyai, and J. W. Cooper, Phys. Rev. A **21**, 1917 (1980).

[50] H. Tatsuno, W. B. Doriese, D. A. Bennett, C. Curceanu, J. W. Fowler, J. Gard, F. P. Gustafsson, T. Hashimoto, R. S. Hayano, J. P. Hays-Wehle *et al.*, J. Low Temp. Phys. **184**, 930 (2016).

[51] T. Åberg, J. P. Briand, P. Chevallier, A. Chetioui, J. P. Rozet, M. Tavernier, and A. Touati, J. Phys. B **9**, 2815 (1976).

[52] W. B. Doriese, P. Abbamonte, B. K. Alpert, D. A. Bennett, E. V. Denison, Y. Fang, D. A. Fischer, C. P. Fitzgerald, J. W. Fowler, J. D. Gard *et al.*, Rev. Sci. Instrum. **88**, 053108 (2017).

[53] S. Okada, D. A. Bennett, C. Curceanu, W. B. Doriese, J. W. Fowler, J. D. Gard, F. P. Gustafsson, T. Hashimoto, R. S. Hayano, S. Hirenzaki *et al.*, Prog. Theor. Exp. Phys. **2016**, 091D01 (2016).

[54] T. Hashimoto, M. Bazzi, D. A. Bennett, C. Berucci, D. Bosnar, C. Curceanu, W. B. Doriese, J. W. Fowler, H. Fujioka, C. Guaraldo *et al.*, IEEE Trans. Appl. Supercond. **27**, 1 (2017).

[55] T. Hashimoto, D. A. Bennett, W. B. Doriese, M. S. Durkin, J. W. Fowler, J. D. Gard, R. Hayakawa, T. Hayashi, G. C. Hilton, Y. Ichinohe *et al.*, J. Low Temp. Phys. **199**, 1018 (2020).

[56] G. Hölzer, M. Fritsch, M. Deutsch, J. Härtwig, and E. Förster, Phys. Rev. A **56**, 4554 (1997).

[57] R. D. Deslattes, E. G. Kessler, P. Indelicato, L. de Billy, E. Lindroth, and J. Anton, Rev. Mod. Phys. **75**, 35 (2003).

[58] R. Diamant, S. Huotari, K. Hämäläinen, R. Sharon, C. C. Kao, and M. Deutsch, Phys. Rev. A **79**, 062511 (2009).

[59] X.-M. Tong, D. Kato, T. Watanabe, H. Shimizu, C. Yamada, and S. Ohtani, Phys. Rev. A **63**, 052505 (2001).

[60] X.-M. Tong and S.-I. Chu, Phys. Rev. A **55**, 3406 (1997).

[61] J. P. Desclaux, Comput. Phys. Commun. **9**, 31 (1975).

[62] P. Indelicato and J. P. Desclaux, *MCDFGME, a Multiconfiguration Dirac Fock and General Matrix Elements Program (Release 2005)* (2005), http://kroll.lkb.upmc.fr/mcdf.

[63] J. P. Santos, F. Parente, S. Boucard, P. Indelicato, and J. P. Desclaux, Phys. Rev. A **71**, 032501 (2005).

[64] D. Gotta, K. Rashid, B. Fricke, P. Indelicato, and L. M. Simons, Eur. Phys. J. D **47**, 11 (2008).

[65] P. Indelicato, Phys. Rev. A **87**, 022501 (2013).

[66] P. Indelicato, S. Boucard, and E. Lindroth, Eur. Phys. J. D **3**, 29 (1998).

[67] J. L. Campbell and T. Papp, At. Data Nucl. Data Tables **77**, 1 (2001).

[68] W. Bambynek, B. Crasemann, R. W. Fink, H. U. Freund, H. Mark, C. D. Swift, R. E. Price, and P. V. Rao, Rev. Mod. Phys. **44**, 716 (1972).

[69] M. Krause, C. J. Nestor, C. J. Sparks, and E. Ricci, Report No. ORNL-5399, 1978.

[70] M. H. Chen, B. Crasemann, and H. Mark, At. Data Nucl. Data Tables **24**, 13 (1979).

[71] M. H. Chen, B. Crasemann, and H. Mark, Phys. Rev. A **21**, 449 (1980).

[72] R. D. Muiño, A. Salin, N. Stolterfoht, A. Arnau, and P. M. Echenique, Phys. Rev. A **57**, 1126 (1998).

[73] M. Grether, A. Spieler, R. Köhrbrück, and N. Stolterfoht, Phys. Rev. A **52**, 426 (1995).